MAGIC matrices: freeform bioprinting materials to support complex and reproducible organoid morphogenesis

Austin J. Graham[1,2], Michelle W.L. Khoo[2], Vasudha Srivastava[1], Sara Viragova[3], Kavita Parekh[4], Cameron D. Morley[4], Malia Bird[1], Paul Lebel[2], Sanjay Kumar[4,5,6], Ophir Klein[3,7], Rafael Gómez-Sjöberg[2,*], Zev J. Gartner[1,2,6,8,*]

[1]Department of Pharmaceutical Chemistry, University of California San Francisco, San Francisco, CA
[2]Chan Zuckerberg Biohub, San Francisco, CA
[3]Department of Orofacial Sciences, University of California San Francisco, San Francisco, CA
[4]Department of Bioengineering, University of California Berkeley, Berkeley, CA
[5]Department of Chemical and Biomolecular Engineering, University of California Berkeley, Berkeley, CA
[6]Department of Bioengineering and Therapeutic Sciences, University of California San Francisco, San Francisco, CA
[7]Department of Pediatrics, Cedars-Sinai Guerin Children's, Los Angeles, CA
[8]Center for Cellular Construction, University of California San Francisco, San Francisco, CA
*Correspondence: zev.garter@ucsf.edu and rafael.gomez@czbiohub.org

Abstract:

Organoids are powerful models of tissue physiology, yet their applications remain limited due to a lack of complex tissue morphology and high organoid-to-organoid structural variability. To address these limitations we developed a soft, composite yield-stress extracellular matrix that supports freeform 3D bioprinting of cell slurries at tissue-like densities. Combined with a custom piezoelectric printhead, this platform allows more reproducible and complex morphogenesis from uniform and spatially organized organoid "seeds." At 4 °C the material exhibits reversible yield-stress behavior to support long printing times without compromising cell viability. When transferred to cell culture at 37 °C, the material cross-links and exhibits similar viscoelasticity and plasticity to basement membrane extracts such as Matrigel. We use this setup for high-throughput generation of intestinal and salivary gland organoid arrays that are morphologically indistinguishable from those grown in pure Matrigel, but exhibit dramatically improved homogeneity in organoid size, shape, maturation time, and budding efficiency. The reproducibility of organoid structure afforded by this approach increases the sensitivity of assays by orders of magnitude, requiring less input material and reducing analysis times. The flexibility of this approach additionally enabled the fabrication of perfusable intestinal organoid tubes. Combined, these advances lay the foundation for the efficient design of complex tissue morphologies in both space and time.

Introduction

In vitro tissue models that reproducibly and scalably recapitulate complex tissue physiology are required for applications in regenerative medicine, disease modeling, and drug testing[1–8]. Organoids have the potential to satisfy these requirements. They are self-organizing tissues derived from stem and progenitor cells incorporate multiple mature cell types and simple morphological features. In order to self-organize, organoids must be derived from the appropriate cellular progenitors and cultured within the appropriate 3D microenvironments, typically laminin-rich extracellular matrix (ECM) gels like Matrigel[9–15]. Even when these requirements are satisfied, however, organoids lack developmental and anatomical contexts that support and constrain their morphogenesis in vivo. Consequently, they lack much of the complex morphology of real tissue and generally suffer from a high degree of structural heterogeneity[16–21]. Though some of this heterogeneity is intrinsic to the stochastic nature of cell and tissue growth and morphogenesis, there are significant external factors such as initial size, composition, and neighboring interfaces that contribute to morphological heterogeneity[22]. These manifest as differences in organoid mass, morphological features, and cell composition, all of which lead to variability in the outcome of experimental perturbations. Variability in turn decreases the statistical significance between experimental conditions, requiring many replicates to identify phenotypes.

To address these challenges, engineering platforms have sought to better control the initial conditions from which organoids emerge. Such platforms include microwell arrays, microphysiological systems (or organs-on-a-chip), and 3D bioprinting. Microwell arrays are screening platforms that emerge from high-density cell aggregates, generally of a composition defined by Poisson statistics, and arranged spatially for straightforward imaging[23–25]. Microwells can improve organoid homogeneity but are generally limited in the eventual size and geometry of the resulting tissue. In microphysiologcial systems, controlled geometries are lithographically patterned on polymeric chips, which are then coated with cells and ECM to generate the microtissue[26–29]. These powerful tools allow for complex tissue geometries, incorporation of multiple cell types, and microfluidic plumbing for exchange of metabolites between tissue and organ compartments. However, the pre-defined geometry and artificial interfaces such as PDMS impose many constraints on the tissue that may impact normal morphogenesis. Additionally, the top-down constraints on geometry imposed by the workflow can incorporate biases on cell and tissue function. Finally, the chip format requires complete reconfiguration for each build iteration, slowing the design-build-test cycle. In contrast, 3D bioprinting comprises a suite of rapid prototyping tools that provides a potentially more flexible platform for generating tissues of defined size, composition and geometry, on-demand and in arbitrary microenvironments[30–38]. However, most applications of bioprinting remain in their infancy and have typically focused on printing non-living biomaterials or composites of hydrogels and cells. Moreover, these efforts mostly focus on controlling the printed geometry of cells and materials in 3D space, rather than the critical importance of the subsequent morphogenesis of these living materials in time. Consequently, little emphasis has been placed on the interaction between printed structures and the spatial, mechanical, and molecular details of the microenvironment that support their morphogenesis[39].

Recently, several applications of printing and patterning technology have attempted to better program cell and organoid morphogenesis by fabricating tissues from cell slurries at tissue-like densities, then embedding these seeds directly into gold-standard ECMs like Matrigel[40–42]. For example, DNA-programmed assembly of cells (DPAC) is a bottom-up method for patterning dense cell slurries in Matrigel and Matrigel-Collagen-I mixtures that has been applied to fibroblast clusters, mammary organoids, and vasculature[43–45]. Cells are first directed to self-assemble on a 2D template and then released into Matrigel as it polymerizes around them. They can then undergo morphogenesis in 3D. While this method is among the highest resolution (on the order of a single cell) method for printing microtissues, it lacks scalability, has limited height resolution, and can be technically arduous. Embedded bioprinting methods such as bioprinting-assisted tissue emergence (BATE) extrudes dense cell slurries directly into liquid Matrigel or collagen to construct large 3D patterns that undergo morphogenesis[46]. These methods potentially address many of the scalability issues presented by DPAC. However, BATE remains limited by Matrigel's steep transition from low-viscosity fluid to highly viscoelastic solid as a function of temperature, which provides only a very narrow time window in which extruded cell slurries conform to the geometry prescribed by the printer. Consequently, BATE remains a manual printing modality and its capacity to support automation and extended print times has not been explored.

To extend available print times, freeform bioprinting has largely turned to granular media such as Carbopol or gelatin microgel slurries which provide improved bioprinting mechanics[47–49]. One central property of these materials is reversible yield-stress behavior, in which the slurry yields in response to the printhead entering the bath and extruding material, then recovers to provide elastic support to the extruded bioink once the nozzle is removed. However, most of these materials are not optimal for long-term cell growth and morphogenesis[50,51]. To provide relevant ECM, several groups have introduced interstitial biomaterials such as collagen I, but collagen I matrices exhibit strain stiffening and generally are not optimal for supporting morphogenesis of epithelial structures[49,52]. In addition, collagen I and ECM mechanics more broadly are known to significantly impact gene expression programs, and indeed epithelial growth and morphogenesis is altered in collagen compared to Matrigel[46,53–56]. Matrigel has several properties that make it unique as a biomaterial for tissue morphogenesis, but poor as a biomaterial for freeform bioprinting. It is rich in laminin, collagen IV and nidogen—the major components of the basement membrane that provide critical polarity signals to tissue supporting their early morphogenesis. Matrigel is also degradable, undergoes plastic deformations at long times scales, and is a viscoelastic biomaterial with a storage modulus significantly lower than typical materials used in 3D bioprinting applications[57]. However, it is a poor support for freeform bioprinting because it behaves as a viscous fluid at 4 °C, while quickly transitioning to a soft hydrogel at 37 °C for cell culture. Therefore, an embedded bioprinting material that combines the advantageous yield-stress properties of microgels with the soft, viscous, elastic, and plastic properties of Matrigel could revolutionize bioprinting of organoids and tissues.

Here we designed and tested an embedded bioprinting material that is composed of alginate microgels and interstitial Matrigel, termed Matrigel-Alginate Granular-Interstitial Composite (MAGIC) matrix. MAGIC matrices employ alginate microgels that are optically transparent and approximately cell-sized, which facilitates yielding behavior, high print fidelity, simple imaging, and organoid expansion. We concurrently used Matrigel as the interstitial material to create a switchable composite matrix that remains liquid at 4 °C to allow for long print times (≥3 h), but cross-links at 37 °C to create a soft, viscoelastic, and viscoplastic environment that is mechanically identical to pure Matrigel across several metrics. Concurrently, to capitalize on the reproducibility, scalability, and automation afforded by 3D printing, we designed a piezoelectric printhead that is linked to a microscope stage and robotic arms that allow for full xyz-control, real-time imaging, and flexible scripted print geometries. This printhead enabled direct aspiration and extrusion of saturated cell slurries exceeding 10^8 cells/mL, minimizing dead volume and required biomass, with a theoretical limit of 0.1 nL delivered volume. This leads to orders-of-magnitude improvements in inter-organoid homogeneity and statistical precision with 100% formation efficiency. The combined result is a flexible organoid bioprinting platform using a simple but powerful biomaterial that can generate both reproducible and complex in vitro tissues.

Results & Discussion

MAGIC matrices are designed to be optimal bioprinting materials at 4 °C and optimal tissue culture materials at 37 °C

We first sought to design a reversible yield-stress material that supports bioprinting at 4 °C and gold-standard morphogenesis at 37 °C. We turned to alginate as an optically transparent biomaterial that is largely inert in mammalian culture. For these reasons, alginate has been employed in both bioprinting and organoid culture applications as a support medium and rheological modifier[52,58–60]. Given our design constraints, we hypothesized that a yield-stress matrix utilizing alginate microgels with interstitial Matrigel would allow for high-fidelity bioprinting at 4 °C and optimal organoid morphogenesis at 37 °C. We termed this material Matrigel-Alginate Granular-Interstitial Composite (MAGIC) matrix.

We characterized MAGIC matrices by shear rheology under conditions designed for bioprinting (4 ˚C) and organoid culture (37 ˚C). We explored matrix compositions having mechanical properties spanning those likely to support both bioprinting and morphogenesis. In addition to pure formulations of alginate and Matrigel we tested six different matrix compositions in all: three different ratios of Matrigel and alginate microgel (AMG) slurry spanning 2:1, 1:1, and 1:2 by volume; and two different polymer weight fractions in the AMG preparation, 0.5 and 1 wt%. As expected, AMG slurries exhibited temperature-independent, but shear stress-dependent viscoelasticity, including yielding at ~10 Pa shear stress (Figure S1). In contrast, pure Matrigel exhibits significant temperature-dependence as it cross-links to form a hydrogel at physiological temperature (Figure S1).

All compositions of MAGIC matrix demonstrated reversible yield-stress behavior at 4 °C, confirming their utility as embedded bioprinting materials (Figure 2A, Figure S1). At rest, they behaved as viscoelastic solids, with G' greater than G'', in contrast to pure Matrigel (Figure S1). However, as shear stress was increased, G'' overtook G', indicating microgel yielding and rearrangement (Figure 2A). These materials remained as reversible yield-stress fluids for as long as they were kept cold, supporting their ability to support long print times. The specific yield-stress of each composition was measured by unidirectional shear tests and fit to a Herschel-Bulkley exponential model (Figure 2B). Despite their molecular similarity, varying MAGIC matrix composition tuned yield-stress values over more than an order of magnitude (Figure S1). This implies that the material can be engineered to fit the needs of a particular print shape or tissue type.

To assess MAGIC matrix behavior under physiological conditions, we next measured viscoelastic properties following cross-linking at 37 °C. At 0.5 wt% alginate, the storage and loss modulus of the composite matrix approached equivalent values to pure Matrigel (Figure 2C). This was true across a range of MAGIC matrix compositions using the lower alginate weight fraction (Figure S1). However, this was not the case with MAGIC matrices composed of 1 wt% AMGs, where viscoelastic properties were dominated by the microgel slurry (Figure 2C, Figure S1).

To arrive at an ideal MAGIC matrix formulation for both bioprinting and morphogenesis, we applied these ECM compositions in organoid growth assays. Organoids isolated from mouse duodenum were passaged by mechanical dissociation and plated in Matrigel or MAGIC matrix domes. Given the sensitivity of crypt budding and lumen expansion to matrix mechanics[11,19,61,62], we measured crypt length as a representative signature of a permissive ECM. After five days in culture we found that a subset of MAGIC matrix compositions yielded organoids that were indistinguishable from those grown in pure Matrigel (Figure 2E,F). However, all compositions of MAGIC matrix using 1 wt% AMGs yielded organoids with shorter crypts (Figure 2E,F). We hypothesized that a combination of stiffness, viscoelasticity, and yield stress may play important roles in organoid morphogenesis. These results also support the need for soft, viscoelastic materials for embedded bioprinting to promote certain aspects of morphogenesis.

We also observed a negative impact on crypt length for MAGIC matrices composed of 0.5 wt% soft microgels for a high microgel-fraction composition, namely 1:2 Matrigel:AMG by added volume. Given that these materials have similar viscoelasticity at 37 °C (Figure 2C), and that organoids grow normally in diluted Matrigel (Figure S2), we hypothesized that time-dependent viscoelasticity or plasticity might play a role in the differences in organoid phenotype between these biomaterials. We therefore measured the creep response of these materials at 37 °C at a 10 Pa applied shear stress over 10 minutes to simulate the forces and timescales of processes such as lumen expansion that influence organoid morphogenesis[63]. Indeed, the creep response was a strong function of material composition, with Matrigel exhibiting the greatest strain rate and highest plasticity (Figure S3). MAGIC matrices comprising soft (0.5 wt%) AMGs, regardless of composition ratio, exhibited similar strain rates that were less than pure Matrigel, but greater than MAGIC matrices comprising stiff (1 wt%) microgels (Figure S3). We quantified this effect as relaxation modulus, which was nearly identical for MAGIC matrices using soft AMGs (Figure 2D). In contrast, stress relaxation was significantly impeded compared to Matrigel for MAGIC matrices using stiff AMGs (Figure 2D). Notably, the plasticity of MAGIC matrices was less than both pure AMG slurry and pure Matrigel for the conditions tested (Figure S3). While it is possible that excessive microgel jamming could also impact organoid growth at large strains, we did not directly observe this behavior. Ultimately, these results suggest that for MAGIC matrices of a given storage and loss moduli, other material properties such as time-dependent viscosity, elasticity, plasticity, and microgel packing may independently inform gastrointestinal organoid morphogenesis.

A piezoelectric printhead enables precise, automated aspiration and extrusion of dense cell slurries

Our results are consistent with a variety of studies that suggest organoid morphogenesis can be highly stereotyped when beginning with volumes of cells embedded in physiologically relevant matrices at tissue-like cell density[41,46,49]. We therefore focused our efforts on bioinks comprising dissociated and strained organoids and cell cultures centrifuged to produce saturated slurries at approximately 10^8 cells/mL[64,65]. We omitted rheological modifiers and generally excluded divalent cations to prevent cell adhesion through calcium-dependent adhesion systems. In addition, we employed microgels that were approximately cell-sized to facilitate self-organization, migration, and diffusion[49,66] (Figure S4). However, we found that reproducible and controlled printing of cell slurries at these densities required designing a printhead that could handle small volumes with high precision, fast pressure ramps, and without excess loss due to tubing and fluidics (i.e. “dead volumes”). Thus, we designed a printhead for direct aspiration and extrusion that employs a piezoelectric actuator that is mechanically coupled to an incompressible fluid via a poly(ether ether ketone) PEEK diaphragm (Figure 3A–B). This allowed voltage applied to the piezoelectric material to control its expansion or contraction, and thus both acquire and deliver precise volumes.

The piezoelectric printhead was mounted on a robotic arm for Z-control of the pipette position, with its XY-position remaining stationary throughout the course of a print but aligned to the optical axis of the microscope using a manual on-axis optical positioner. Micron-scale resolution of the print XY-position and shape was achieved using the microscope stage, which held the print plate. Microscope integration provided real-time imaging during the printing process, which allowed rapid identification and diagnosis of printing issues should they occur. Bioink was loaded by directly aspirating a user-specified volume from a 384-well sample plate, so that only the printed volume was loaded – this could be beneficial for precious samples such as biopsies or challenging organoid populations where it can be difficult to generate sufficient volume of cell slurry for loading syringes typically used in commercial bioprinters. An electronic valve toggled fluidic connection of the printhead to an incompressible fluid reservoir, allowing it to be filled, cleaned, or purged, and then sealed for single-ended printing operation. The entire process was controlled using MATLAB integrating control of the microscope, stage motion, and fluidics. Custom printing protocols can be scripted for maximum repeatability, efficiency, and iterative troubleshooting.

High-viscosity ink droplets are challenging to print in viscoelastic yield-stress fluids due to a complex interplay of soft matter physics and fluid dynamics[67,68]. For example, inertial and drag forces on the ink can lead to a tailing effect, where ink is pulled as a continuous stream from the tip while it is removed from the support bath. To combat this, we leveraged the printer's ability to rapidly control applied voltage in the piezo printhead to "break" the cell slurry by applying a small back-pressure and z-displacement, generally attenuating this effect (Figure 3C). We then applied this aspiration, extrusion, and tail-breaking program to script an automated spheroid bioprinting array. Using commercially available plastic micropipettes with 1 mm OD and 125 µm ID mounted onto the piezoelectric printhead, we first demonstrated that a Caco2 cell slurry bioink could be delivered to create spheroids (Figure 3D) of customizable dimensions. Spheroid volume was an approximately linear function of extrusion step, which was controlled through changes in voltage applied to the piezo material (Figure 3E). In general, around 90% of cells were viable after dissociation and slurry preparation as measured by trypan blue exclusion. In addition, Caco2 spheroids underwent lumenization and inflation, as is expected for these tissues in 3D culture[69], implying the dissociation and printing process did not substantially impact cell viability. The cell slurry could also be viably printed using 75 or 200 µm ID micropipettes, highlighting the flexibly of the setup at various print resolutions. Thus, the piezoelectric printhead affords high volume precision to work with small numbers of potentially precious cells as well as rapid, flexible control over bioink behavior using applied voltage. To our knowledge, this is the first demonstration of applying a piezoelectric material to control direct aspiration and extrusion of dense cell slurries.

Having established conditions for the automated preparation of 3D tissues using Caco-2 cells, we next bioprinted mouse small intestine organoid arrays. Primary cells were harvested, cultured, passaged, and dissociated into a cell slurry as previously described[46]. To assess the impact of print geometry on organoid behavior, we systematically varied either inter-organoid spacing or z-depth within the MAGIC matrix support bath. Organoids were printed with an average diameter of 200 µm. Those printed with 250 µm inter-bolus spacing compacted and fused over time, leading to one large organoid (Figure 3F). This fusion is known to occur in manually seeded Matrigel dome culture as well[19,41]. Organoids spaced 500 µm remained distinct and appeared to undergo normal morphogenesis through at least 6 days of culture (Figure S5). However, 5 days later, crypts only appeared at the periphery of the organoid array, while the central organoid remained compacted and without crypts while showing signs of necrosis. (Figure 3E). We hypothesize that this could be caused either by nutrient scavenging by outermost organoids, or microgel compaction as the surrounding organoids expand. Organoids printed ≥750 µm apart did not have noticeable growth impacts, as they grew similar in size and showed crypt formation around their entire circumference (Figure 3F). Printing depth also had a profound effect on organoid health, with organoids printed closer to the ECM-media interface growing the largest and forming the most crypts (Figure 3G)[70]. Together, these results highlight the importance of initial conditions on organoid morphogenesis and imply that such effects could impact experimental results when working with organoids in manual 3D culture. Ultimately, the automation and standardization afforded using the piezoelectric printhead and MAGIC matrices allows rapid exploration of a wide parameter space, with initial culture conditions tailored for a desired assay or application.

MAGIC matrix supports the rapid self-organization of multiple organoid types following bioprinting

Having established initial conditions supporting controlled organoid growth, we next assessed whether organoid arrays cultured in MAGIC matrix exhibited characteristic features of their self-organization. We assessed the morphology of organoids using confocal microscopy, taking advantage of the optical transparency of the matrix and the consistent z-position of all organoids in the printed array. Live imaging of a membrane-localized tdTomato reporter revealed crypt budding and protrusion within 2–3 days after printing in 96-well microplates, occurring with faster and more regular timing than seen in traditional dome cultures (Figure 4B). In addition, *Lgr5+* stem cells were effectively positioned toward the base of these crypt structures (Figure 4C). Fixed gut organoids stained positive for mature epithelial cell types, including Paneth cells (lysozyme) and enteroendocrine cells (chromogranin-A) (Figure 4D,E; Figure S6). Cohesive and contiguous cell borders were marked with E-cadherin. 3D reconstruction of organoids in MAGIC matrix revealed that crypts radiated in all directions from the organoid, suggestive of 3D morphogenesis unencumbered by neighboring interfaces (Figure 4F,G,H).

To establish the generality of MAGIC matrix for bioprinting and morphogenesis of different epithelial tissues we derived organoids from mouse submandibular salivary gland, an ectoderm-derived tissue, as opposed to the endoderm-derived gut. These organoids were cultured in Matrigel domes and then harvested as a single-cell slurry in an identical fashion to the small intestine organoids (Figure 4I). Bioprinted salivary gland organoid arrays self-organized and exhibited characteristic multi-lobular structures within 3 days after printing (Figure 4J). Salivary gland organoids stained positive for ductal and basal epithelial markers, keratins 8 and 14, respectively (Figure 4K). The entire process of primary salivary gland isolation, organoid preparation, bioprinting, and immunofluorescence validation took approximately 4 weeks with no protocol optimization, highlighting the generality of this material and printing platform for a variety of tissue and organoid models.

Bioprinted organoid arrays dramatically improve assay sensitivity

The heterogeneity of traditional organoid culture limits their potential in a variety of assays. Differences in organoid size, morphological features such as number of crypts, and position across multiple z-planes obscures subtle phenotypes that are only revealed after analyzing dozens to hundreds of individual organoids. The regularity of bioprinted organoid arrays in MAGIC matrix could dramatically improve the sensitivity of such assays. We quantified the timing and regularity of small intestinal organoid morphogenesis when bioprinted in MAGIC matrix compared to traditional culture methods. Over the course of 5 days, bioprinted organoids synchronously self-organized, initially into lumenized cysts that then underwent budding morphogenesis to form crypts (Figure 5A). By contrast, over 5 days, manually seeded organoids showed significant heterogeneity in size and maturity over the same timeframe (Figure 5B,C). Furthermore, for a given amount of time post-seeding, bioprinted organoid arrays underwent more extensive and uniform morphogenesis, exhibiting a greater number of crypts with decreased variance compared to manually seeded organoids (Figure 5D)[71]. Organoids grown in manually seeded cultures using MAGIC matrix as opposed to pure Matrigel showed no difference in crypt number (Figure 5D), indicating that the bioprinting method itself leads to this improved maturity.

Improved homogeneity in organoid structure should improve assays aiming to detect subtle phenotypes, for example in chemical or genetic screens. To test this idea we treated organoids with a gamma-secretase inhibitor (DAPT), which is known to increase the number of *Atoh1+*

secretory progenitors in mouse gut organoids (Figure 5E)[72,73]. Using an *Atoh1*^{CreERT2}*:Rosa26*^{tdTomato} reporter line, we treated bioprinted and manually seeded organoid cultures with DAPT at the time of seeding and imaged after 3 days. In manually seeded organoids, differences in overall tdTomato signal acquired by confocal microscopy were obscured by heterogeneity in organoid position and size (Figure 5F). In contrast, there was a clear increase in tdTomato signal for DAPT-treated organoids in bioprinted arrays (Figure 5G). Quantifying the volume of tdTomato-positive signal in each condition revealed that while there was a statistically significant increase in signal for both bioprinted and manual-seeded organoids in treated vs. untreated conditions, the distribution and variance in the data were substantially improved using bioprinted arrays (Figure 5H). Moreover, the variance in bioprinted organoids is more normally distributed, leading to an order-of-magnitude decreased coefficient of variance.

To more precisely quantify how bioprinted arrays improved assay sensitivity, we performed bootstrapping on the bioprinted and manually seeded populations to calculate p-value as a function of the number of paired organoid comparisons (treated vs. untreated). In the bioprinted arrays, we achieved p-values below 0.05 after comparing only 5 organoids; in traditional organoid cultures, 45 comparisons were required to reach the same statistical significance (Figure 5I). P-values for bioprinted organoids continued to decrease with additional comparisons approaching 10^{-10} after 45 comparisons – the same number of organoids necessary to achieve a p-value of 0.05 in manually seeded organoids.

Rapid and flexible production of 3D perfusable gut tubes

In addition to enabling more rapid and homogeneous formation of organoids in a standard assay format, MAGIC matrices and the piezoelectric printhead present opportunities to create more structurally complex and functional 3D tissues from organoid slurries. One architecture common to many tissues types is a tubular geometry. Many tissues spontaneously lumenize to form tubes from an initially cylindrical morphology when placed in laminin-rich ECM[41,45,46]. We therefore optimized process parameters for bioprinting organoid cylinders, with the hypothesis that MAGIC matrices would support their spontaneous lumenization, and therefore, their perfusion. Cylinder diameter could be independently tuned using either extrusion speed or stage speed, providing multiple engineering controls, some unique to the piezo printhead (Figure 6A). Bioprinted cylinders underwent similar self-organization and compaction followed by growth and morphogenesis as observed in spheroid arrays. Using gut organoid slurries, tubes lumenized and began forming crypts radially around the long axis of the gut tube 2–3 days after printing. Individual crypts showed characteristic stem cell and Paneth cell self-organization (Figure 6B, C).

The emergence of patent lumens in printed tissues provides an opportunity to interface these complex culture models with perfusion systems. Using glass capillaries piercing the tissue lumen, we pushed fluid through the tubes, thereby clearing internal cellular debris. We observed radial expansion of the perfused tubes when pressurized, indicating that the boundaries of the tissue remained flexible and devoid of interfaces having non-physiological stiffness (Figure 6D, Supplementary Movies 1–3). By oscillating fluid flow through the tube, we could simulate cyclic expansion and shrinking of the tubes as would occur during peristalsis. Thus, this setup combines the advantages of apical lumen access, a key feature of microphysiological systems, while maintaining a free basal surface that ultimately can be interfaced with other tissue types.

Discussion

Through key innovations in biomaterials for free form bioprinting and printhead design, we have created a generalizable and scalable platform for 3D organoid and tissue fabrication. In contrast to most embedded bioprinting materials optimized only for supporting printed shapes, we have additionally designed and optimized materials to support tissue self-organization. Our work identified a critical role for complex rheological parameters as well as the chemical components necessary for a permissive growth environment. Despite their complex rheological properties at 4 ˚C and 37 ˚C, MAGIC matrices are relatively simple in design, employing off-the-shelf and well-characterized constituents. Moreover, they are readily tunable by changing the size and composition of the granular medium as well as the interstitial material. To fully utilize these materials, we developed a piezoelectric printhead allowing precise aspiration and extrusion of cell slurries at tissue-like densities, thereby allowing tissues to autonomously self-organize without the stochasticity typically associated with tissue growth and differentiation. Combined, the matrix and printhead enable rapid prototyping and controlled extrusion of delicate materials while minimizing dead volumes. Importantly, the overall design will allow further optimization of extrusion rate and delivered cell volumes that are difficult or impossible to perform using pneumatics or syringe pumps.

The size and modulus of the microgel fraction of granular media are known to impact cell growth and behavior[74,75]. Here, we demonstrate that a combination of rheological properties including plasticity, stress relaxation, and yield-stress may comprise new dimensions to consider when designing ECMs for bioprinting and tissue culture[76]. Given these results, we proceeded with bioprinting experiments using a MAGIC matrix composition of 1:1 Matrigel-to-AMGs by added volume prepared at 0.5 wt% alginate. These materials balanced expected gut organoid morphogenesis at 37 °C with a low yield-stress at 4 °C (~1 Pa) that supported both print fidelity and long-term tissue health. This yield-stress is much lower than many reported embedded printing materials, which may contribute to their ineffectiveness as cell culture materials[57]. Notably, the desired yield-stress of MAGIC matrices can be tuned for a given application independent of the bulk viscoelasticity during cell growth. In addition, the viscous, elastic, and plastic properties of alginate could be tuned independent of Matrigel chemical composition by changing the degree of cross-linking or weight fraction. Depending on the specific formulation, this may lead to changes in time-dependent stress relaxation, which provides another engineering handle for controlling tissue morphogenesis. Ultimately, the simultaneous simplicity and flexibility of this biomaterial should enable broad use for 3D culture applications.

Both endoderm and ectoderm derived epithelial tissues could be rapidly generated using piezoelectric bioprinting into MAGIC matrix. These organoids showed increased homogeneity by a number of metrics, including growth, morphogenesis, and maturation rate. In previous studies, small intestine organoids exhibiting any number of crypt structures have been deemed “assay-ready,” meaning the functional epithelial cell types and morphologies are established[25]. Engineering methods for generating organoid arrays that rely on single-cell dissociation and sorting for Lgr5+ stem cells generate assay-ready organoids in 5 days or more[20,25]. Comparatively, bioprinted organoids were assay-ready in 2-3 days. Similarly, submandibular salivary gland organoids could be bioprinted and cultured in high-throughput arrays using the exact same material and protocol, requiring no optimization. Budding in salivary gland organoids is driven by strong cell-matrix interactions and weak cell-cell interactions[77,78]; these results imply that for this MAGIC matrix composition, these strong cell-matrix interactions were not disrupted by decreased Matrigel concentration or the presence of microgels. These results again highlight the broad utility of this platform for numerous tissue types.

Combined, these technologies have important implications for the application of organoids in high-throughput biology, drug screens, and personalized medicine. To demonstrate the potential of this approach in high-throughput biology we leveraged scripting and automation to generate organoid arrays that underwent more rapid and more uniform morphogenesis than previously described methods. These arrays were amenable to both live and fixed imaging. Moreover, these organoids could potentially be collected for dissociation, sorting, and sequencing. By controlling the initial conditions of tissue growth and eliminating extrinsic sources of heterogeneity, we demonstrated dramatic improvements assay sensitivity. For example, we decreased the number of observations required to identify a statistically significant phenotype by an order of magnitude compared to traditional culture. As the number of observations increased to the double digits, the organoid arrays prepared here provide assay sensitivities many of orders of magnitude better than traditional culture methods. Based on a conservative estimation of our experiments, 16–36 organoids could be generated per well of a 96-well microplate, easily yielding thousands of organoids on a single plate. This means that a greater number of comparisons can be made, with greater sensitivity, in a single high-throughput experiment. Therefore, this platform simultaneously requires fewer organoids and improves statistical precision, presenting opportunities to work with rare cell types or primary patient biopsies for drug screens. It will also prove critical for assays with complex readouts and long culture times, such as human stem cell-derived organoids.

Finally, we present progress toward future construction of more complex and in vivo-like 3D microphysiological systems by perfusing bioprinted gut tubes. The regularity and scalability of these models could be combined with established high-throughput pipelines for screening drugs or gene therapies using organ-on-chip platforms, but without the drawbacks of artificial interfaces and geometries. Ultimately, our material and bioprinting platform combines multiple advances to take a large and meaningful step toward addressing the need for more complex and reproducible in vitro models of living tissues.

Figure 1. MAGIC extracellular matrices are embedded bioprinting materials that enable construction of uniform and complex organoid architectures. A. By controlling for initial conditions such as cell number, media access, and organoid spacing, bioprinting platforms could facilitate 3D organoid assays in high-throughput. **C.** MAGIC matrix comprises of an alginate microgel granular support and a basement membrane hydrogel interstitium. This compositionally simple material supports embedded bioprinting support at 4 °C and tissue morphogenesis at 37 ˚C. **D.** Organoid slurries printed into pure basement membrane extract at 4 °C form distorted features and settle to the bottom of the dish due to insufficient mechanical support (Movie S1). Organoids slurry printed into MAGIC matrices at 4 °C conform to the desired morphology due to its reversible yield-stress properties. **E.** Sequential brightfield images demonstrating organoid array bioprinting, in which the printhead enters cold MAGIC matrix, extrudes organoid slurry, and is then removed from the matrix, leaving a geometrically and spatially controlled feature behind. These slurries undergo self-organization to form mature organoids. Scale bars = 500 μm.

Figure 2. MAGIC matrices behave as reversible yield-stress materials at 4 °C and as viscoelastic and viscoplastic cell culture matrices at 37 °C. **A.** At 4 °C, oscillatory amplitude sweeps at 1 Hz reveal that various MAGIC matrix compositions behave as yield-stress materials, indicated by G' and G'' cross-over. **B.** Unidirectional shear rate measurements reveal that at 4 °C, MAGIC matrices behave as Herschel-Bulkley fluids whose yield-stresses can be calculated using a power law model. **C.** At 37 °C, the storage and loss modulus of MAGIC matrices prepared from 0.5 wt% AMGs are indistinguishable from pure Matrigel, whereas they are significantly greater for MAGIC matrices prepared from 1 wt% AMGs. **D.** Creep experiments demonstrate that for a given applied stress, 0.5 wt% MAGIC matrices relax in a fashion similar to pure Matrigel, whereas 1 wt% MAGIC matrices are less compliant. **E.** Gut organoids grown in pure Matrigel (left) or MAGIC matrices (right) at day 5 after seeding. Scale bars = 100 μm. **F.** Quantification of organoid crypt length as a function of matrix composition. A combination of alginate weight fraction and microgel packing in MAGIC matrices can impact morphogenesis compared to pure Matrigel. For all rheological experiments, data shown are mean ± SEM from $n = 3$ independently prepared replicates. For crypt length measurements, data shown are mean ± SEM of $n \geq 45$ crypts on ≥ 10 organoids per matrix condition. * = $p \leq 0.05$; ** = $p \leq 0.01$; **** = $p \leq 0.0001$; ns = not significant determined by one-way ANOVA with Tukey's multiple comparisons (**B**, **C**) or Dunnett's multiple comparisons (**F**).

Figure 3. A piezoelectric printhead enables precise aspiration and extrusion of cell slurries, and can be programmed to generate automated organoid arrays. **A.** Cartoon rendering of the piezoelectric bioprinter setup, which is mounted on an inverted microscope for real-time imaging and feedback. **B.** Box outlines cartoon of the printhead and piezoelectric material, which are linked via an incompressible fluid to either draw or dispense volume based on applied voltage. **C.** Representative 3D renderings of bioprinted spheroids with and without the tail-breaking script enabled by piezoelectric bioprinting through rapid changes in applied voltage and printhead position. Scale bars = 200 μm. **D.** Representative fluorescent 3D renderings of bioprinted Caco2 tissues. Delivered cell slurry volume can be tuned by changing applied voltage, which changes the step size of piezo displacement. Data are representative of at least $n = 10$ individual tissues. **E.** Spheroid volume measured using segmented 3D confocal z-stack images of GFP-expressing Caco2 cell slurries. Organoids compact and self-organize over the first 3 days and subsequently grow. In all cases, spheroid and tissue size correlate approximately linearly with initial extrusion step size (statistics in SI). Insets show representative brightfield images of spheroids from that day with scale bars = 100 μm. Data represent $n \geq 10$ individual tissues per extrusion condition. **F.** Bioprinted gut organoids printed with 250, 500, or 1250 μm inter-spheroid spacing. Tissues printed too close together fuse (left) or show increased necrosis (middle), whereas tissues printed far enough apart appear to develop independently (right). **G.** Bioprinted gut organoids printed at different depths within the MAGIC matrix (500 μm, 1000 μm, or 1500 μm from the cover glass). Spheroids printed deeper in the matrix suffer from increased "tailing," and resultant structures can be observed in out-of-focus planes. In **F,G** scale bars = 1 mm.

Figure 4. MAGIC matrices promote the self-organization of organoids derived from both endodermal and ectodermal tissues. **A.** Live imaging of gut organoids with membrane *tdTomato+* 2 days after bioprinting in MAGIC matrix. **B.** Live imaging of an *Lgr5-eGFP* reporter 3 days after bioprinting in MAGIC matrix. Inset shows overlaid brightfield and fluorescence image. Scale bar = 500 μm. **C, D.** Maximum intensity projection of DAPI- or ECAD- and GFP-stained gut organoids 3 days after bioprinting. Scale bar = 1 mm. **E.** Detail of a bioprinted organoid as in D and E. Scale bar = 100 μm. **F, G.** 3D renderings reveal characteristic self-organization of differentiated cell types and crypts protruding in all directions. **H.** Live imaging of membrane *tdTomato+* mouse salivary gland organoids cultured in Matrigel domes. Scale bar = 480 μm. **I.** Live imaging of bioprinted salivary gland organoid arrays. Scale bar = 1 mm. **J.** Immunofluorescence of fixed bioprinted salivary gland organoids showing presence of both basal (keratin 14) and ductal (keratin 8) cells. Scale bars = 100 μm.

Figure 5. High-throughput organoid bioprinting decreases assay time and increases sensitivity and reproducibility. **A.** Live imaging of bioprinted gut organoid arrays following printing and after 2 and 5 days of culture. **B.** Manually seeded organoids at day 5 grow at variable z planes and **C,D** have more variable size and maturity (as measured by organoid area and number of crypts per organoid). Scale bars = 500 μm. For **C**, data shown are mean ± SEM of n ≥ 190 organoids; for **D**, data shown are mean ± SEM of n ≥ 30 organoids. **** = $p < 0.0001$; ns = not determined by one-way ANOVA with Dunnett's multiple comparisons. **E.** Experimental outline of phenotypic assay for inhibition of gamma-secretase. **F, G.** Live imaging of manually seeded and bioprinted organoids treated with and without the gamma-secretase inhibitor DAPT. Red fluorescence indicates *Atoh1+* secretory progenitors. Scale bars = 500 μm. **H.** Total red fluorescence volume per organoid in treated and untreated conditions. For bioprinted arrays, data shown are mean ± SD of n = 45 organoids per condition. For manually seeded organoids, data shown are mean ± SD of n ≥ 135 organoids per condition. **** = $p < 0.0001$ determined by non-parametric t-test. **I.** Bootstrapping analysis of statistical significance between treated and untreated conditions for either bioprinted or manually seeded organoids as a function of number of paired comparisons. Inset demonstrates that bioprinted organoids improve statistical precision by many orders of magnitude for a given number of observations.

Figure 6. Fabrication and perfusion of tubular tissues amenable to perfusion. A. Quantification of bioprinted tube diameter as a function of both stage translation speed and extrusion step speed. As with spheroids, bioprinted tubes first undergo compaction and self-organization followed by growth and lumenization. Initial and final tube diameter are roughly linear functions of extrusion step speed for a given stage translation speed (statistics in SI). Insets show representative brightfield images of tubes from that day with scale bar = 500 μm. Data shown are n = 3 bioprinted tubes per condition. **B.** Live imaging (left) and immunofluorescence imaging (right) of mature bioprinted gut organoid tubes stained to reveal crypt morphology and characteristic stem cell and Paneth cell self-organization. Scale bars = 200 μm. **C.** 3D renderings of fixed gut organoid tubes showing crypts protruding in all directions outward from the central organoid body. **D.** Visual representation of replicated peristalsis experiment in which a bioprinted gut tube is perfused and fluid flowed through the tube lumen. Scale bar = 500 μm. **E.** Plot of tube diameter as a function of time as fluid is pressurized using the syringe. Gray shaded areas represent positive pressure applied to the syringe.

Materials and Methods

Materials and methods are provided in the supplement.

Data and Code Availability

All source data will be made available upon peer-reviewed publication. Custom MATLAB, R, and Fiji scripts will be publicly made available through GitHub upon peer-reviewed publication or can be provided upon request.

Acknowledgements

We thank the members of the Gartner Lab, Klein Lab, and CZ Biohub Bioengineering Group for their valuable suggestions. We thank Sandra Montes-Olivas for guidance in the use of her MATLAB crypt counting software. We thank Dr. Kevin Healy for providing rheological equipment. We thank This work was funded by the Chan Zuckerberg Investigator Program to Z.J.G., the UCSF Center for Cellular Construction (DBI-1548297), and the NIDDK (R01DK126376). A.J.G. was supported by a Chan Zuckerberg Biohub Collaborative Postdoctoral Fellowship. V.S. was supported by the Zena Werb Memorial Fellowship through the Helen Diller Family Cancer Center at UCSF. FACS was performed on a BD Aria 3, supported in part by HDFCCC Laboratory for Cell Analysis Shared Resource Facility through a grant from NIH (P30CA082103).

Author Contributions

A.J.G. and Z.J.G. conceptualized the embedded bioprinting material design and application. A.J.G., M.W.L.K., P.L., R.G.S., and Z.J.G. conceptualized the bioprinter instrumentation. M.W.L.K., P.L., and R.G.S. designed and built the bioprinter hardware and wrote the software. A.J.G., V.S., and S.V. performed primary cell isolation, culture, immunofluorescence, and organoid experiments. A.J.G. and M.W.L.K. performed experiments to identify optimal bioprinting parameters. M.W.L.K. wrote custom scripts for bioprinting organoid arrays. A.J.G. and V.S. wrote custom scripts for microscopy and statistical analysis. K.P., C.M., and S.K. consulted on and provided experimental assistance with material characterization. S.V. and O.K. consulted on and provided experimental assistance with organoid isolation, characterization, and application. A.J.G. and Z.J.G. wrote the manuscript, with review and feedback from all other authors.

Declaration of Interest

A.J.G., R.G.S., and Z.J.G. are co-inventors on a patent regarding the design and application of the embedded bioprinting material and piezoelectric printhead (application no. to be shared upon publication).

References

1. Dekkers, J. F. *et al.* A functional CFTR assay using primary cystic fibrosis intestinal organoids. *Nat Med* **19**, 939–945 (2013).

2. Clevers, H. Modeling Development and Disease with Organoids. *Cell* **165**, 1586–1597 (2016).

3. Koike, H. *et al.* Modelling human hepato-biliary-pancreatic organogenesis from the foregut–midgut boundary. *Nature* **574**, 112–116 (2019).

4. Driehuis, E., Kretzschmar, K. & Clevers, H. Establishment of patient-derived cancer organoids for drug-screening applications. *Nat Protoc* **15**, 3380–3409 (2020).

5. Jiang, S. *et al.* An Automated Organoid Platform with Inter-organoid Homogeneity and Inter-patient Heterogeneity. *Cell Reports Medicine* **1**, 100161 (2020).

6. Hofer, M. & Lutolf, M. P. Engineering organoids. *Nat Rev Mater* **6**, 402–420 (2021).

7. Wolf, K. J., Weiss, J. D., Uzel, S. G. M., Skylar-Scott, M. A. & Lewis, J. A. Biomanufacturing human tissues via organ building blocks. *Cell Stem Cell* **29**, 667–677 (2022).

8. Viragova, S. *et al.* Inverse agonists of retinoic acid receptor/retinoid X receptor signaling as lineage-specific antitumor agents against human adenoid cystic carcinoma. *JNCI: J. Natl. Cancer Inst.* **115**, 838–852 (2023).

9. Sato, T. *et al.* Single Lgr5 stem cells build crypt-villus structures in vitro without a mesenchymal niche. *Nature* **459**, 262–265 (2009).

10. Cerchiari, A. E. *et al.* A strategy for tissue self-organization that is robust to cellular heterogeneity and plasticity. *Proc National Acad Sci* **112**, 2287–2292 (2015).

11. Gjorevski, N. *et al.* Designer matrices for intestinal stem cell and organoid culture. *Nature* **539**, 560–564 (2016).

12. Broguiere, N. *et al.* Growth of Epithelial Organoids in a Defined Hydrogel. *Adv. Mater.* **30**, e1801621 (2018).

13. Aisenbrey, E. A. & Murphy, W. L. Synthetic alternatives to Matrigel. *Nat Rev Mater* 1–13 (2020) doi:10.1038/s41578-020-0199-8.

14. Rezakhani, S., Gjorevski, N. & Lutolf, M. P. Extracellular matrix requirements for gastrointestinal organoid cultures. *Biomaterials* **276**, 121020 (2021).

15. Hunt, D. R. *et al.* Engineered Matrices Enable the Culture of Human Patient-Derived Intestinal Organoids. *Adv Sci* **8**, 2004705 (2021).

16. Brassard, J. A. & Lutolf, M. P. Engineering Stem Cell Self-organization to Build Better Organoids. *Cell Stem Cell* **24**, 860–876 (2019).

17. Beck, L. E. *et al.* Systematically quantifying morphological features reveals constraints on organoid phenotypes. *Cell Syst* **13**, 547-560.e3 (2022).

18. Lukonin, I., Zinner, M. & Liberali, P. Organoids in image-based phenotypic chemical screens. *Exp. Mol. Med.* **53**, 1495–1502 (2021).

19. Tallapragada, N. P. *et al.* Inflation-collapse dynamics drive patterning and morphogenesis in intestinal organoids. *Cell Stem Cell* **28**, 1516-1532.e14 (2021).

20. Serra, D. *et al.* Self-organization and symmetry breaking in intestinal organoid development. *Nature* **569**, 66–72 (2019).

21. Bues, J. *et al.* Deterministic scRNA-seq captures variation in intestinal crypt and organoid composition. *Nat Methods* 1–8 (2022) doi:10.1038/s41592-021-01391-1.

22. Srivastava, V. *et al.* Configurational entropy is an intrinsic driver of tissue structural heterogeneity. *bioRxiv* 2023.07.01.546933 (2023) doi:10.1101/2023.07.01.546933.

23. Sockell, A. *et al.* A microwell platform for high-throughput longitudinal phenotyping and selective retrieval of organoids. *Cell Syst.* **14**, 764-776.e6 (2023).

24. Lin, F. *et al.* Mechanically enhanced biogenesis of gut spheroids with instability-driven morphomechanics. *Nat. Commun.* **14**, 6016 (2023).

25. Brandenberg, N. *et al.* High-throughput automated organoid culture via stem-cell aggregation in microcavity arrays. *Nat Biomed Eng* **4**, 863–874 (2020).

26. Huh, D. *et al.* Reconstituting Organ-Level Lung Functions on a Chip. *Science* **328**, 1662–1668 (2010).

27. Jalili-Firoozinezhad, S. *et al.* A complex human gut microbiome cultured in an anaerobic intestine-on-a-chip. *Nat Biomed Eng* **3**, 520–531 (2019).

28. Nikolaev, M. *et al.* Bioengineering microfluidic organoids-on-a-chip. (2020) doi:10.21203/rs.3.pex-903/v1.

29. Nikolaev, M. *et al.* Homeostatic mini-intestines through scaffold-guided organoid morphogenesis. *Nature* **585**, 574–578 (2020).

30. Madden, L. R. *et al.* Bioprinted 3D Primary Human Intestinal Tissues Model Aspects of Native Physiology and ADME/Tox Functions. *Iscience* **2**, 156–167 (2018).

31. Hinton, T. J. *et al.* Three-dimensional printing of complex biological structures by freeform reversible embedding of suspended hydrogels. *Sci Adv* **1**, e1500758 (2015).

32. Bakht, S. M. *et al.* 3D Bioprinting of Miniaturized Tissues Embedded in Self-Assembled Nanoparticle-Based Fibrillar Platforms. *Adv. Funct. Mater.* **31**, (2021).

33. Daly, A. C., Davidson, M. D. & Burdick, J. A. 3D bioprinting of high cell-density heterogeneous tissue models through spheroid fusion within self-healing hydrogels. *Nat Commun* **12**, 753 (2021).

34. Lee, Y. B. *et al.* Induction of Four-Dimensional Spatiotemporal Geometric Transformations in High Cell Density Tissues via Shape-Changing Hydrogels. *Adv. Funct. Mater.* **31**, 2010104 (2021).

35. Lawlor, K. T. *et al.* Cellular extrusion bioprinting improves kidney organoid reproducibility and conformation. *Nat Mater* **20**, 260–271 (2021).

36. McLoughlin, S. T., McKenna, A. R. & Fisher, J. P. 4d Bioprinting via Molecular Network Contraction for Membranous Tissue Fabrication. *Adv. Healthc. Mater.* e2300642 (2023) doi:10.1002/adhm.202300642.

37. Song, M. J. *et al.* Bioprinted 3D outer retina barrier uncovers RPE-dependent choroidal phenotype in advanced macular degeneration. *Nat Methods* **20**, 149–161 (2023).

38. Urciuolo, A. *et al.* Hydrogel-in-hydrogel live bioprinting for guidance and control of organoids and organotypic cultures. *Nat Commun* **14**, 3128 (2023).

39. Daly, A. C., Prendergast, M. E., Hughes, A. J. & Burdick, J. A. Bioprinting for the Biologist. *Cell* **184**, 18–32 (2021).

40. Ho, D. L. L. *et al.* Large-Scale Production of Wholly Cellular Bioinks via the Optimization of Human Induced Pluripotent Stem Cell Aggregate Culture in Automated Bioreactors. *Adv Healthc Mater* 2201138 (2022) doi:10.1002/adhm.202201138.

41. Todhunter, M. E. *et al.* Programmed synthesis of three-dimensional tissues. *Nat Methods* **12**, 975–981 (2015).

42. Gjorevski, N. *et al.* Tissue geometry drives deterministic organoid patterning. *Science* **375**, eaaw9021 (2022).

43. Hughes, A. J. *et al.* Engineered Tissue Folding by Mechanical Compaction of the Mesenchyme. *Dev Cell* **44**, 165-178.e6 (2018).

44. Cabral, K. A. *et al.* Simple, Affordable, and Modular Patterning of Cells using DNA. *J Vis Exp* (2021) doi:10.3791/61937.

45. Cabral, K. A. *et al.* Programming the Self-Organization of Endothelial Cells into Perfusable Microvasculature. *Tissue Eng Pt A* **29**, 80–92 (2023).

46. Brassard, J. A., Nikolaev, M., Hübscher, T., Hofer, M. & Lutolf, M. P. Recapitulating macro-scale tissue self-organization through organoid bioprinting. *Nat Mater* **20**, 22–29 (2021).

47. Bhattacharjee, T. *et al.* Writing in the granular gel medium. *Sci Adv* **1**, e1500655 (2015).

48. Morley, C. D. *et al.* Quantitative characterization of 3D bioprinted structural elements under cell generated forces. *Nature Communications* 1–9 (2019) doi:10.1038/s41467-019-10919-1.

49. Reynolds, D. S. *et al.* Microporogen-Structured Collagen Matrices for Embedded Bioprinting of Tumor Models for Immuno-Oncology. *Adv. Mater.* e2210748 (2023) doi:10.1002/adma.202210748.

50. O'Bryan, C. S., Kabb, C. P., Sumerlin, B. S. & Angelini, T. E. Jammed Polyelectrolyte Microgels for 3D Cell Culture Applications: Rheological Behavior with Added Salts. *Acs Appl Bio Mater* **2**, 1509–1517 (2019).

51. Morley, C. D., Tordoff, J., O'Bryan, C. S., Weiss, R. & Angelini, T. E. 3D aggregation of cells in packed microgel media. *Soft Matter* **16**, 6572–6581 (2020).

52. Kajtez, J. *et al.* Embedded 3D Printing in Self-Healing Annealable Composites for Precise Patterning of Functionally Mature Human Neural Constructs. *Adv Sci* 2201392 (2022) doi:10.1002/advs.202201392.

53. Chaudhuri, O., Cooper-White, J., Janmey, P. A., Mooney, D. J. & Shenoy, V. B. Effects of extracellular matrix viscoelasticity on cellular behaviour. *Nature* **584**, 535–546 (2020).

54. Yui, S. *et al.* YAP/TAZ-Dependent Reprogramming of Colonic Epithelium Links ECM Remodeling to Tissue Regeneration. *Cell Stem Cell* **22**, 35-49.e7 (2018).

55. Mandal, K. *et al.* Soft Hyaluronic Gels Promote Cell Spreading, Stress Fibers, Focal Adhesion, and Membrane Tension by Phosphoinositide Signaling, Not Traction Force. *ACS Nano* **13**, 203–214 (2019).

56. Kobayashi, S. *et al.* Collagen type I-mediated mechanotransduction controls epithelial cell fate conversion during intestinal inflammation. *Inflamm. Regen.* **42**, 49 (2022).

57. Lei, I. M. *et al.* Soft Hydrogel Shapeability via Supportive Bath Matching in Embedded 3D Printing. *Adv. Mater. Technol.* **8**, (2023).

58. Chaudhuri, O. *et al.* Hydrogels with tunable stress relaxation regulate stem cell fate and activity. *Nat Mater* **15**, 326–334 (2016).

59. Elosegui-Artola, A. *et al.* Matrix viscoelasticity controls spatiotemporal tissue organization. *Nat. Mater.* **22**, 117–127 (2023).

60. Nerger, B. A. *et al.* 3D Hydrogel Encapsulation Regulates Nephrogenesis in Kidney Organoids. *Adv. Mater.* e2308325 (2024) doi:10.1002/adma.202308325.

61. Pérez-González, C. *et al.* Mechanical compartmentalization of the intestinal organoid enables crypt folding and collective cell migration. *Nat Cell Biol* **23**, 745–757 (2021).

62. Yang, Q. *et al.* Cell fate coordinates mechano-osmotic forces in intestinal crypt formation. *Nat Cell Biol* 1–12 (2021) doi:10.1038/s41556-021-00700-2.

63. Tee, S.-Y., Bausch, A. R. & Janmey, P. A. The mechanical cell. *Curr. Biol.* **19**, R745–R748 (2009).

64. Groll, J. *et al.* A definition of bioinks and their distinction from biomaterial inks. 1–6 (2018) doi:10.1088/1758-5090/aaec52.

65. Sun, W. *et al.* The bioprinting roadmap. *Biofabrication* **12**, 022002 (2020).

66. Morley, C. D. *et al.* Spatiotemporal T cell dynamics in a 3D bioprinted immunotherapy model. *Bioprinting* e00231 (2022) doi:10.1016/j.bprint.2022.e00231.

67. Zhu, J. & Cai, L.-H. All-Aqueous Printing of Viscoelastic Droplets in Yield-Stress Fluids. *Acta Biomater* (2022) doi:10.1016/j.actbio.2022.09.031.

68. Becker, M., Gurian, M., Schot, M. & Leijten, J. Aqueous Two-Phase Enabled Low Viscosity 3D (LoV3D) Bioprinting of Living Matter. *Adv. Sci.* **10**, 2204609 (2023).

69. Navis, A. & Bagnat, M. Developing pressures: fluid forces driving morphogenesis. *Curr. Opin. Genet. Dev.* **32**, 24–30 (2015).

70. Raghavan, S. *et al.* Decoupling diffusional from dimensional control of signaling in 3D culture reveals a role for myosin in tubulogenesis. *J Cell Sci* **123**, 2877–2883 (2010).

71. Montes-Olivas, S. *et al.* In-silico and in-vitro morphometric analysis of intestinal organoids. *PLOS Comput. Biol.* **19**, e1011386 (2023).

72. McKinley, K. L. *et al.* Cellular aspect ratio and cell division mechanics underlie the patterning of cell progeny in diverse mammalian epithelia. *eLife* **7**, e36739 (2018).

73. Castillo-Azofeifa, D. *et al.* Atoh1+ secretory progenitors possess renewal capacity independent of Lgr5+ cells during colonic regeneration. *Embo J* **38**, (2019).

74. Muir, V. G. *et al.* Influence of Microgel and Interstitial Matrix Compositions on Granular Hydrogel Composite Properties. *Adv Sci* 2206117 (2023) doi:10.1002/advs.202206117.

75. Morley, C. D., Ding, E. A., Carvalho, E. M. & Kumar, S. A Balance Between Inter- and Intra-Microgel Mechanics Governs Stem Cell Viability in Injectable Dynamic Granular Hydrogels. *Adv. Mater.* e2304212 (2023) doi:10.1002/adma.202304212.

76. Carvalho, E. M. & Kumar, S. Lose the stress: Viscoelastic materials for cell engineering. *Acta Biomater.* **163**, 146–157 (2023).

77. Wang, S., Matsumoto, K., Lish, S. R., Cartagena-Rivera, A. X. & Yamada, K. M. Budding epithelial morphogenesis driven by cell-matrix versus cell-cell adhesion. *Cell* (2021) doi:10.1016/j.cell.2021.05.015.

78. Cazares, O., Haque, A. S. & Klein, O. D. Salivary gland: A budding genius. *Dev Cell* **56**, 2271–2272 (2021).

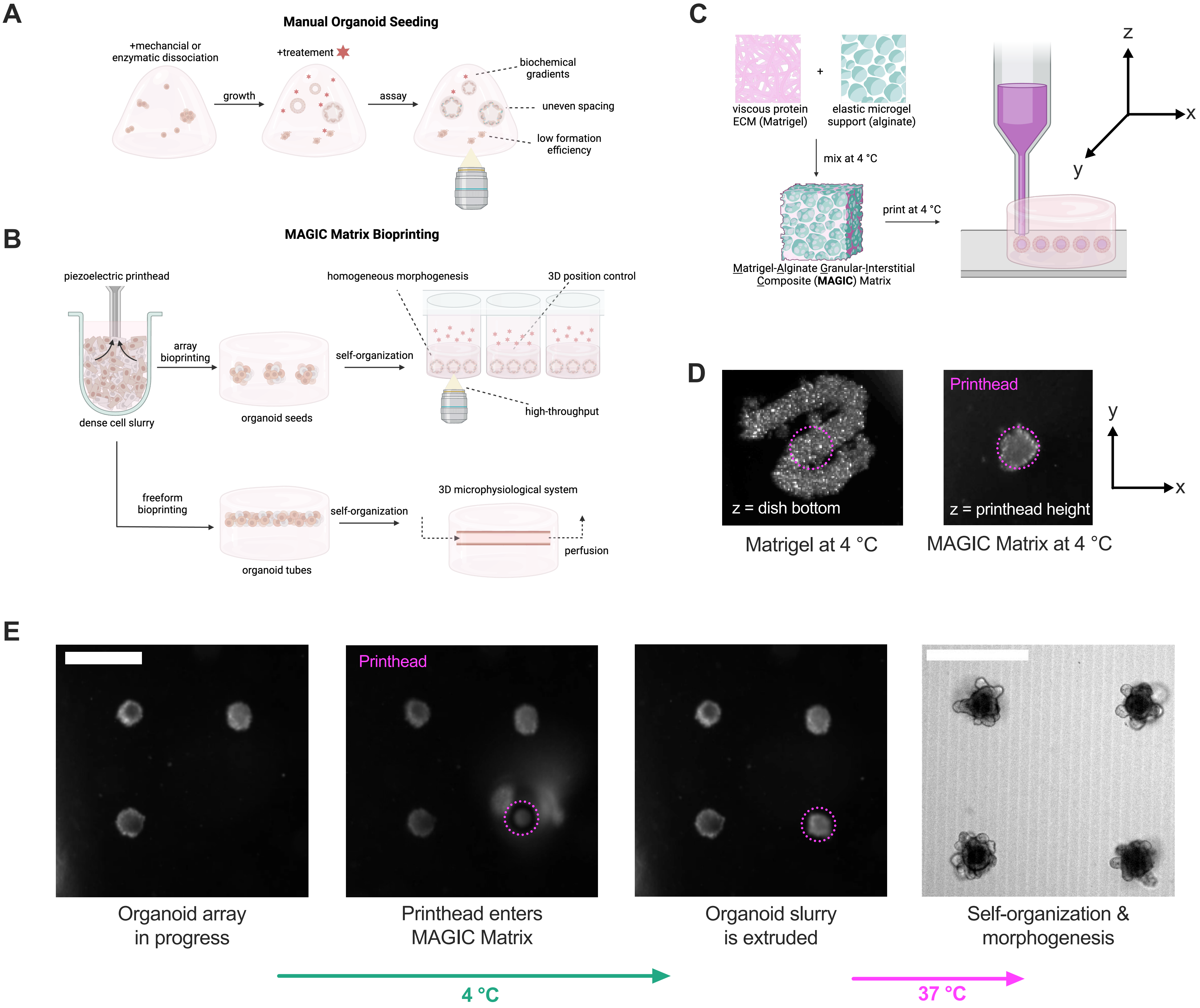
A
Manual Organoid Seeding
+mechancial or enzymatic dissociation
growth
+treatement
assay
biochemical gradients
uneven spacing
low formation efficiency
B
MAGIC Matrix Bioprinting
piezoelectric printhead
dense cell slurry
array bioprinting
organoid seeds
self-organization
homogeneous morphogenesis
3D position control
high-throughput
freeform bioprinting
organoid tubes
self-organization
3D microphysiological system
perfusion
C
viscous protein ECM (Matrigel)
+
elastic microgel support (alginate)
mix at 4 °C
Matrigel-Alginate Granular-Interstitial Composite (MAGIC) Matrix
print at 4 °C
z
x
y
D
z = dish bottom
Matrigel at 4 °C
Printhead
z = printhead height
MAGIC Matrix at 4 °C
y
x
E
Organoid array in progress
Printhead
Printhead enters MAGIC Matrix
Organoid slurry is extruded
Self-organization & morphogenesis
4 °C
37 °C

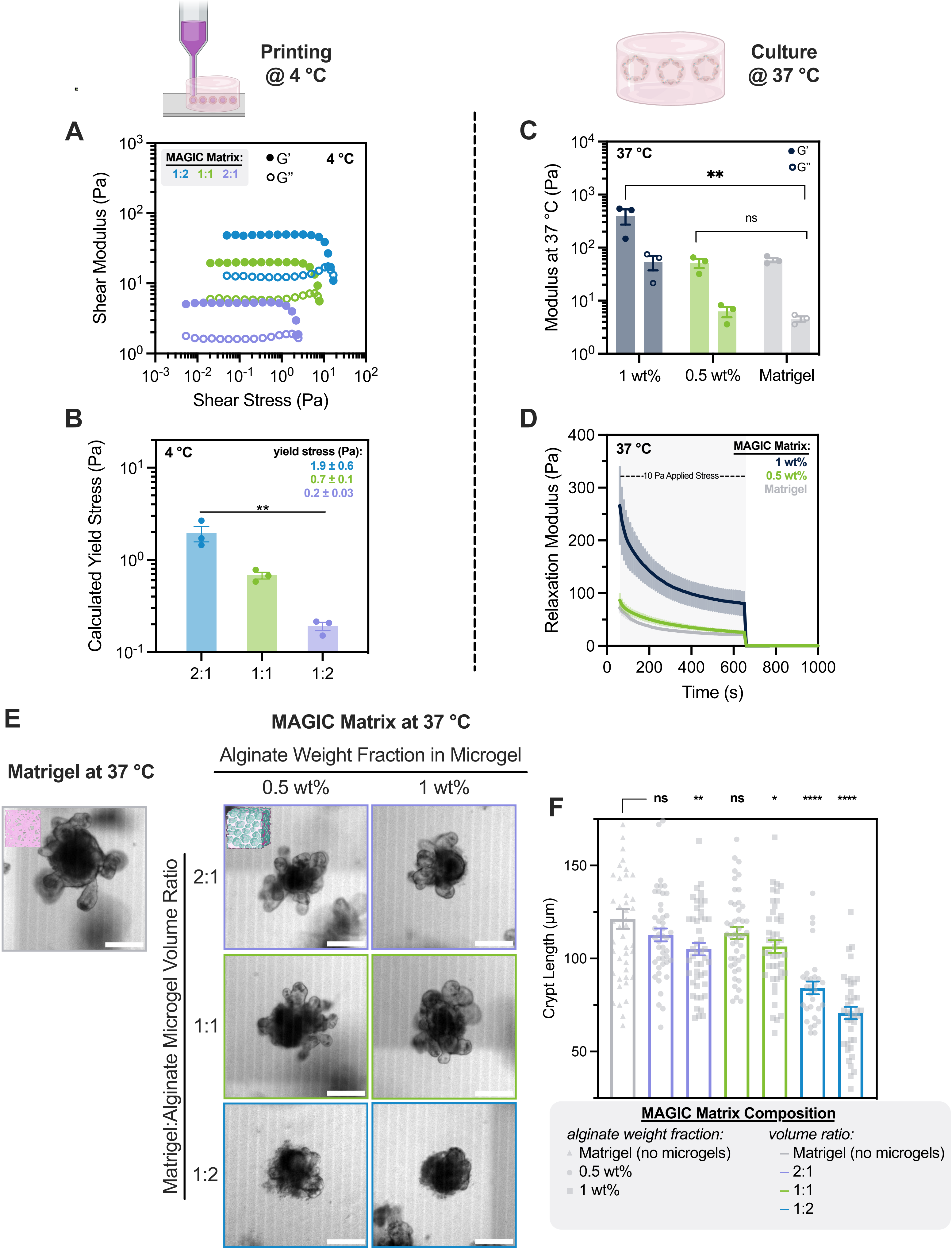
Printing
@ 4 °C
Culture
@ 37 °C
A
MAGIC Matrix:
1:2 1:1 2:1
● G'
○ G"
4 °C
Shear Modulus (Pa)
10^3
10^2
10^1
10^0
10^{-3} 10^{-2} 10^{-1} 10^0 10^1 10^2
Shear Stress (Pa)
B
4 °C
yield stress (Pa):
1.9 ± 0.6
0.7 ± 0.1
0.2 ± 0.03
**
Calculated Yield Stress (Pa)
10^1
10^0
10^{-1}
2:1
1:1
1:2
C
37 °C
● G'
○ G"
**
ns
Modulus at 37 °C (Pa)
10^4
10^3
10^2
10^1
10^0
1 wt%
0.5 wt%
Matrigel
D
37 °C
MAGIC Matrix:
1 wt%
0.5 wt%
Matrigel
10 Pa Applied Stress
Relaxation Modulus (Pa)
400
300
200
100
0
0 200 400 600 800 1000
Time (s)
E
MAGIC Matrix at 37 °C
Matrigel at 37 °C
Alginate Weight Fraction in Microgel
0.5 wt%
1 wt%
Matrigel:Alginate Microgel Volume Ratio
2:1
1:1
1:2
F
ns ** ns * **** ****
Crypt Length (μm)
150
100
50
MAGIC Matrix Composition
alginate weight fraction:
▲ Matrigel (no microgels)
● 0.5 wt%
■ 1 wt%
volume ratio:
– Matrigel (no microgels)
– 2:1
– 1:1
– 1:2

A
B
Outlet port
PEEK diaphragm
Fluid-filled cavity
Piezoelectric actuator
cell slurry
or
125 um plastic tip
C
tail-breaking script
without
with
y
x
z
y
D
Piezo Extrusion Step Size (µm)
0.01
0.05
0.1
0.2
Day 0
GFP
E
self-organization
growth & expansion
Day 0
Day 3
Day 7
10^8
10^7
10^6
10^5
Bolus Volume (µm^3)
0.01
0.1
1
Extrusion Step (µm)
F
250 µm
Day 6
500 µm
Day 11
1250 µm
Day 11
G
500 µm
Day 4
1000 µm
Day 4
1500 µm
Day 4

A
mTOMATO
B
LGR5
C
DAPI
D
ECAD
LGR5
E
ECAD
DAPI
LYZ
F
ECAD
X (µm)
Y (µm)
Z (µm)
G
LGR5
LYZ
X (µm)
Y (µm)
Z (µm)
0 50 100 150 200 250 300 350 400 450
H
mTOMATO
I
J
fix, stain, image
KRT14
KRT8

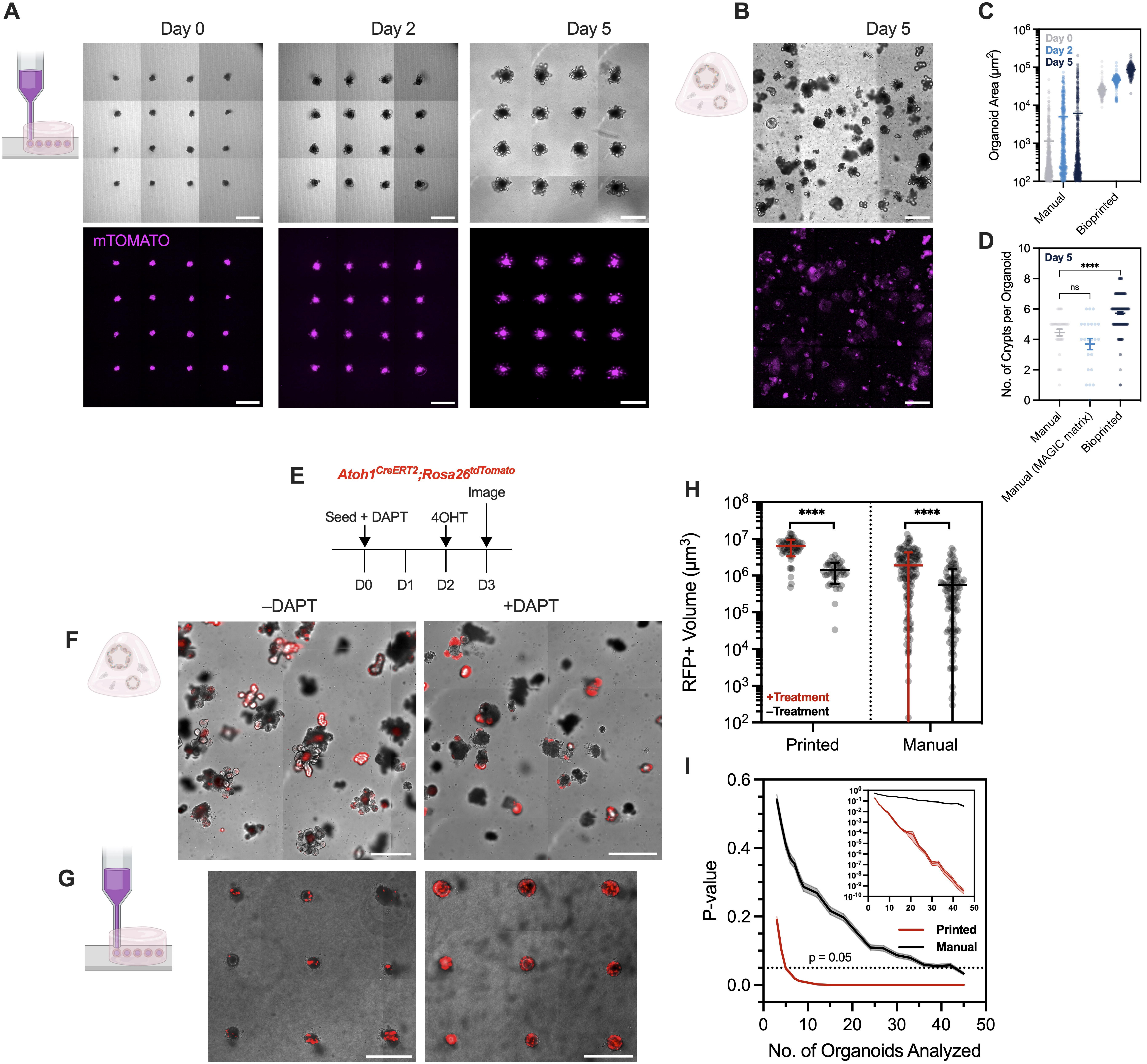
A
Day 0
Day 2
Day 5
mTOMATO
B
Day 5
C
Organoid Area (μm²)
Day 0
Day 2
Day 5
10⁶
10⁵
10⁴
10³
10²
Manual
Bioprinted
D
Day 5
No. of Crypts per Organoid
****
ns
10
8
6
4
2
0
Manual
Manual (MAGIC matrix)
Bioprinted
E
Atoh1CreERT2;Rosa26tdTomato
Image
Seed + DAPT
4OHT
D0
D1
D2
D3
F
–DAPT
+DAPT
G
H
RFP+ Volume (μm³)
10⁸
10⁷
10⁶
10⁵
10⁴
10³
10²
****
****
+Treatment
–Treatment
Printed
Manual
I
P-value
0.6
0.4
0.2
0.0
p = 0.05
Printed
Manual
0
10
20
30
40
50
No. of Organoids Analyzed
10⁰
10⁻¹
10⁻²
10⁻³
10⁻⁴
10⁻⁵
10⁻⁶
10⁻⁷
10⁻⁸
10⁻⁹
10⁻¹⁰

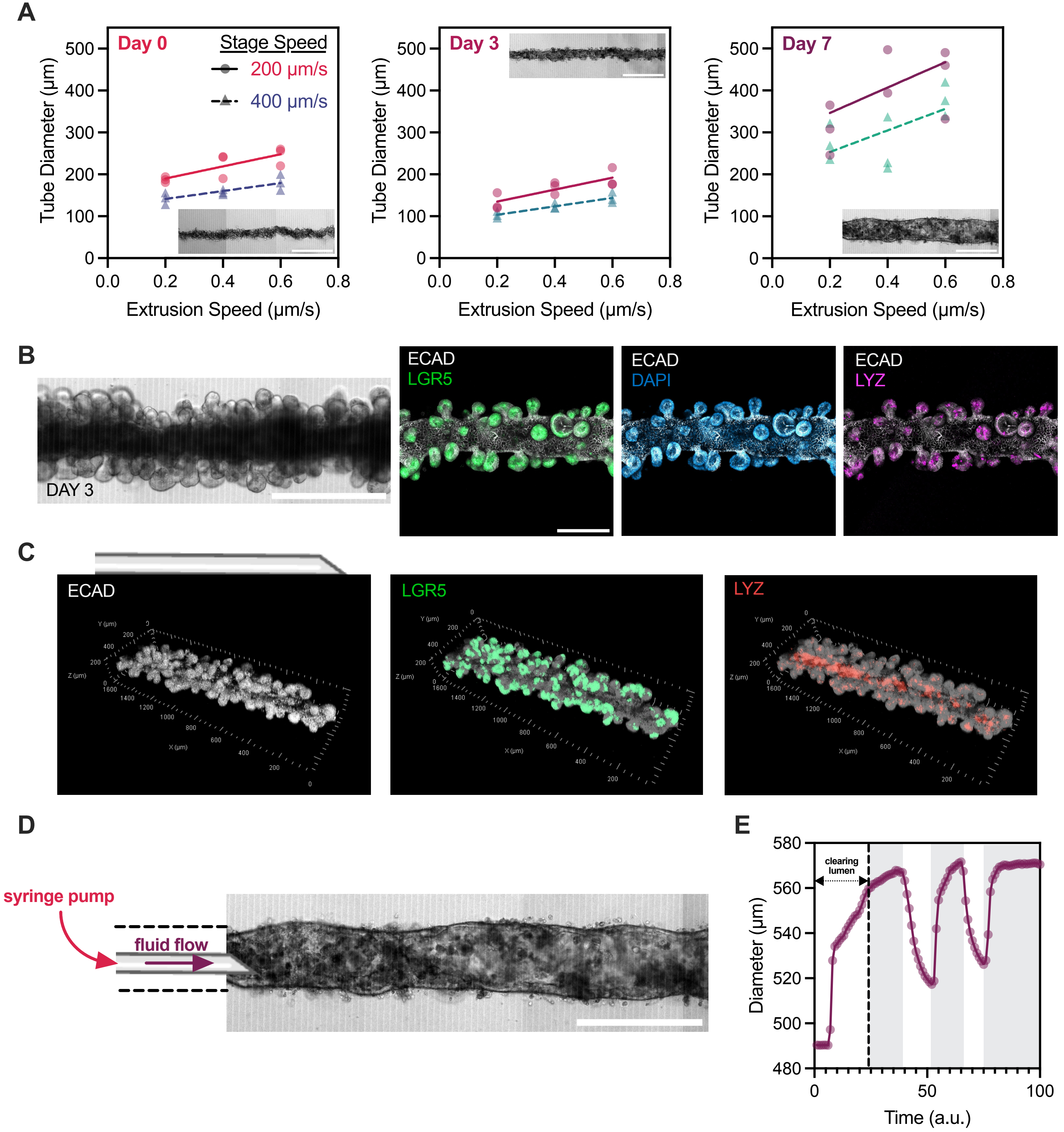
A
Day 0
Stage Speed
200 μm/s
400 μm/s
Tube Diameter (μm)
500
400
300
200
100
0
0.0
0.2
0.4
0.6
0.8
Extrusion Speed (μm/s)
Day 3
Day 7
B
DAY 3
ECAD
LGR5
ECAD
DAPI
ECAD
LYZ
C
ECAD
LGR5
LYZ
Y (μm)
Z (μm)
X (μm)
D
syringe pump
fluid flow
E
clearing lumen
Diameter (μm)
580
560
540
520
500
480
0
50
100
Time (a.u.)